Revisiting the Fundamental Analytical Solutions of Heat and Mass Transfer: The Kernel of Multirate and Multidimensional Diffusion

Quanlin Zhou[1], Curtis M. Oldenburg[1], Jonny Rutqvist[1], and Jens T. Birkholzer[1]

[1] Energy Geosciences Division, Lawrence Berkeley National Laboratory, Berkeley, CA, USA

Correspondence to: Q. Zhou, qzhou@lbl.gov

Abstract

There are two types of analytical solutions of temperature/concentration in and heat/mass transfer through boundaries of regularly shaped 1-D, 2-D, and 3-D blocks. These infinite-series solutions with either error functions or exponentials exhibit highly irregular but complementary convergence at different dimensionless times, t_d. In this paper, approximate solutions were developed by combining the error-function-series solutions for early times and the exponential-series solutions for late times and by using time partitioning at the switchover time, t_{d0}. The combined solutions contain either the leading term of both series for normal-accuracy approximations (with less than 0.003 relative error) or the first two terms for high-accuracy approximations (with less than 10^{-7} relative error) for 1-D isotropic (spheres, cylinders, slabs) and 2-D/3-D rectangular blocks (squares, cubes, rectangles, and rectangular parallelepipeds). This rapid and uniform convergence for rectangular blocks was achieved by employing the same time partitioning with individual dimensionless times for different directions and the product of their combined 1-D slab solutions. The switchover dimensionless time was determined to minimize the maximum approximation errors. Furthermore, the analytical solutions of first-order heat/mass flux for 2-D/3-D rectangular blocks were derived for normal-accuracy approximations. These flux equations contain the early-time solution with a three-term polynomial in $\sqrt{t_d}$ and the late-time solution with the limited-term exponentials for rectangular blocks. The heat/mass flux equations and the combined temperature/concentration solutions form the ultimate kernel for fast simulations of multirate and multidimensional heat/mass transfer in porous/fractured media with millions of low-permeability blocks of varying shapes and sizes.

1 Introduction

The fundamental analytical solutions for heat conduction and solute diffusion in regularly shaped porous-medium blocks have been available for different boundary and initial conditions (Carslaw & Jaeger, 1959; Crank, 1975; Hahn & Ozisik, 2012; Holman, 1990). For one-dimensional (1-D) conduction/diffusion in slabs, cylinders, and spheres, the solutions of temperature/concentration contain an infinite series of trigonometric and exponential functions developed by either the method of separation of variables or the Laplace transformation. This exponential-series type of solution converges super-slowly for very small dimensionless times, i.e., the

Fourier Number, t_d, but satisfactorily for moderate and large t_d. The second type of solution contains an infinite series of error functions or error-function complements. This type of solution is obtained using the Laplace transform with the expansion in negative exponentials (Crank, 1975). The second type of solution converges quite rapidly for all except large t_d. Crank (1975) focused on the complementary convergence properties and numerical evaluation of both types of series solutions separately. However, fast evaluation of combined solutions over the entire time domain for $t_d=[0,\infty]$ is needed for practical numerical simulations of heat and mass transfer in porous and fractured media.

For 2-D and 3-D rectangular blocks (rectangular corners, rectangles, rectangular parallelepipeds, squares, cubes), the multidimensional temperature/concentration solutions are the product of 1-D slab solutions in the different directions, as long as their initial condition can be written in terms of the product of 1-D initial conditions (Carslaw & Jaeger, 1959; Crank, 1975; Newman, 1936). The convergence of the exponential-series solutions is extremely poor at small t_d because of the multiplication of two or three infinite series. One method for improving convergence is to develop alternative Green's functions (for the response at a location caused by a point source of heat at a different location) with numerical and analytical integration (Beck & Cole, 2007; Beck et al., 2008; Cole & Yen, 2001; Crittenden & Cole, 2002). The other method is the so-called time-partitioning method, in which the time interval of integration is partitioned into short and long-time subintervals where the Green's functions are approximated by their small and large-time representations (Beck et al., 1992, 2004, 2006; McMasters et al., 2002; Yen et al., 2002). Both methods can have very high accuracy of approximation, relatively efficient calculations, and flexibility in handling the first, second, and third types of boundary conditions, as well as internal heat generation. However, both methods are complicated and may not meet the computational efficiency required for modeling heat and mass transfer in the subsurface with millions to billions of low-permeability aggregates and matrix blocks, whose local boundary conditions are simple and homogeneous.

Following the two types of fundamental solutions of dimensionless heat/mass transferred through block boundaries (Crank, 1975), Zhou et al. (2017) developed the unified-form heat/mass flux equations to greatly simplify the calculations of cumulative and transient diffusive flux through boundaries of 1-D isotropic and 2-D/3-D rectangular blocks for $t_d=[0,\infty]$. The flux equation contains the early-time solution with a three-term polynomial in $\sqrt{t_d}$ and the late-time solution with the leading term of the infinite exponential series for slabs, cylinders, and spheres. The switchover dimensionless time was determined for each shape of these isotropic and 2-D/3-D anisotropic blocks to minimize the maximum approximation errors, which were less than 0.2%. For rectangular blocks, the coefficients of the polynomial depend only on dimensionless area-to-volume ratio and aspect ratios. The late-time solutions

follow the truncated exponential series, the number of which depends on the degree of geometric anisotropy of the blocks. The format and the coefficients of the early-time solutions for rectangular blocks were obtained by fitting the exact exponential-series solutions for different aspect ratios. However, rigorous mathematical derivation is needed to promote the applications of these flux equations to the broader heat/mass transfer community. In addition, for highly anisotropic rectangular blocks, uniform convergence is needed to make the analytical solutions practical for use in large-scale numerical modeling applications.

Possibly because of the lack of the heat/mass flux equations for 2-D and 3-D blocks, only 1-D equations have been used to couple local conduction/diffusion in low-permeability aggregates and matrix blocks (slabs, cylinders, and spheres) with global advection and dispersion in high-permeability channels or fractures for analytical modeling of heat/mass transfer in the subsurface porous or fractured media. The exact solutions over the entire time domain have been obtained by using the Laplace transform for modeling pressure propagation in aquifer-aquitard systems and fractured reservoirs (e.g., Cihan et al., 2011; Moench, 1984; Zhou et al., 2009), solute and tracer transport in fractured reservoirs (e.g., Becker & Charbeneau, 2000; Carrera et al., 1998; Maloszewski & Zuber, 1985, 1990, 1993; Moench, 1989, 1991, 1995; Reimus et al., 2003; Sudicky & Frind, 1982; Tang et al., 1981; Zhou et al., 2006, 2007), and heat transfer in fractured reservoirs (e.g., Jung & Pruess, 2012; Lauwerier, 1955). The simplification of 2-D and 3-D aggregates and matrix blocks to 1-D might produce large simulation errors for hydraulic, solute, and thermal diffusion (e.g., van Genuchten & Dalton, 1986). Furthermore, the moderate and large-time behavior of solute diffusion or back-diffusion has often been handled by truncating the exponential series in the time domain (Haggerty & Gorelick, 1995; Haggerty et al., 2000, 2001, 2004; Silva et al., 2009; Willmann et al., 2008) or by using first-order dual-porosity models (Barenblatt et al., 1960; Brusseau et al., 1989; Coats & Smith, 1964; Guan et al., 2008; Pruess & Narasimhan, 1985; van Genuchten & Wierenga, 1976; Warren & Root, 1963; Zhou et al., 2017), without consideration of the early-time behavior. Therefore, the fundamental heat/mass flux equations for 2-D/3-D rectangular blocks are needed for accurate modeling of subsurface heat and mass transfer.

In this paper, we combine the error-function-series and exponential-series solutions of temperature/concentration and heat/mass flux to form approximate solutions that are fast-converging and continuous over the entire time domain. The time partitioning between the early and the late-time solutions using a switchover dimensionless time results in normal-accuracy approximations (less than 0.003 relative error) with the leading term of both series and high-accuracy approximations (less than 10^{-7} relative error) with the first two terms of both series. Rapid and uniform convergence is achieved using the optimally determined switchover time for 1-D isotropic

blocks. For 2-D and 3-D rectangular blocks, this convergence is achieved using the product of the combined solutions of 1-D slab in all directions, with the time partitioning based on their own dimensionless time. Alternatively, the leading term for the early-time solution of the combined heat/mass flux equations is a three-term polynomial in $\sqrt{t_d}$ for each shape of blocks. The coefficients of this polynomial are either available for 1-D isotropic blocks in the literature (Crank, 1975; Zhou et al., 2017) or derived for 2-D/3-D rectangular blocks in this research. For the latter, the derived coefficient only depends on the dimensionless area-to-volume ratio and aspect ratios, showing the physical insights into the effects of block geometry on the early-time solutions. These combined flux equations for conduction/diffusion in multidimensional blocks can be easily used to couple with large-scale heat/mass advection and dispersion for analytical and numerical modeling. This coupling will be demonstrated in two companion papers, with multirate (to represent effects of different block shape and size) and multidimensional (to represent the different sets of fractures and corresponding matrix blocks) diffusion, for modeling pressure propagation, heat flow, and solute transport in the subsurface and beyond the scope of this technique report. Here, we present the derivation of the combined early and late-time temperature/concentration and heat/mass flux equations followed by some illustrative example calculations.

2 Fundamental Solutions for Temperature Distributions

Heat conduction in solid blocks, heat conduction in porous-medium blocks, solute diffusion in porous-medium blocks, and solute diffusion in fluid-filled blocks share the same forms of solutions of temperature/concentration when dealing with dimensionless time and spatial variables, regardless of the specific definitions of the thermal/solute diffusivity (D) and their orders of magnitude difference. In what follows, we focus on heat conduction and transfer in solid and porous-medium blocks.

In this section, we are interested in the solutions of the temperature distributions in various geometrically isotropic (sphere, cylinder, slab, square, cube) and anisotropic (rectangle and rectangular parallelepiped) blocks that are assumed to be of homogeneous and isotropic thermal properties (e.g., thermal conductivity). For each block shape, we list the two standard types of solutions: an infinite error-function series and an infinite exponential series, and then develop combined solutions over the entire time domain by taking advantage of the fast convergence of both series in their respective time regimes.

2.1 Temperature Solutions for 1-D Isotropic Blocks

For a 1-D isotropic block (slab, sphere, cylinder), the block has a half-spacing or radius of l, a uniform initial temperature of T_0 and a constant surface temperature of T_1 at $x=l$. The block center at $x=0$ has a no-flow condition. Let us introduce two dimensionless primary variables:

$$x_d = x/l, \quad t_d = Dt/l^2, \tag{1}$$

where x is the single spatial variable, t is the time, and D is the thermal diffusivity of the block. Let us also introduce two dimensionless dependent variables:

$$T_d = (T - T_0)/(T_1 - T_0), \tag{2a}$$

$$M_d = M_t/M_\infty = (T_{av} - T_0)/(T_1 - T_0), \tag{2b}$$

where T is the temperature, $T_d(x_d, t_d)$ is the dimensionless temperature, and $M_d(t_d)$ is the dimensionless cumulative heat transferred through the block boundary at the time t. M_t denotes the total amount of heat that has entered the block from its boundary at time t, and M_∞ denotes the corresponding quantity after infinite time. M_d also represents the dimensionless average block temperature or dimensionless cumulative heat flux, while $T_{av}(t_d)$ is the block average temperature.

The governing equation for heat conduction using the dimensionless variables can be written (Haggerty & Gorelick, 1995):

$$\frac{\partial T_d}{\partial t_d} = \frac{1}{x_d^{\nu-1}} \frac{\partial}{\partial x_d} \left(x_d^{\nu-1} \frac{\partial T_d}{\partial x_d} \right), \tag{3a}$$

where ν denotes the dimensionality of the block, with $\nu = 1, 2, 3$ representing slab, cylinder, and sphere, respectively. The boundary conditions are

$$T_d = 1 \text{ at } x_d = 1, \tag{3b}$$

$$\partial T_d/\partial x_d = 0 \text{ at } x_d = 0. \tag{3c}$$

For equation (3), the first type of solution of temperature distribution contains an infinite trigonometric-exponential series for slabs and spheres or an infinite Bessel-function-exponential series for cylinders, which can be obtained using the method of separation of variables (Carslaw & Jaeger, 1959; Crank, 1975). These solutions for slab-like, spherical, and cylindrical blocks are, respectively:

$$T_d = 1 - 2\sum_{n=1}^{\infty} \frac{2(-1)^{n-1}}{(2n-1)\pi} \exp\left[-\left(\frac{2n-1}{2} \right)^2 \pi^2 t_d \right] \cos\left(\frac{2n-1}{2} \pi x_d \right), \tag{4a}$$

$$T_d = 1 - 2\sum_{n=1}^{\infty} \frac{(-1)^{n-1}}{n\pi x_d} \exp\left(-n^2 \pi^2 t_d \right) \sin(n\pi x_d), \tag{4b}$$

$$T_d = 1 - 2\sum_{n=1}^{\infty} \frac{1}{\beta_n J_1(\beta_n)} \exp\left(-\beta_n^2 t_d \right) J_0(\beta_n x_d), \tag{4c}$$

where J_0 and J_1 are the Bessel function of the first kind of the zero and first-order, respectively, and β_n are the zeros of $J_0(x)$.

The second type of solution for spheres and slabs contains an infinite series of error functions or error-function complements. These solutions are obtained using expansion in negative exponentials (Crank, 1975, p. 22) and can be interpreted as reflection and superposition using the basic similarity

solution. This similarity solution for a semi-infinite slab is $T_d = \text{erfc}\frac{1-x_d}{2\sqrt{t_d}} = \text{erfc}\frac{x'_d}{2\sqrt{t_d}}$ with x'_d as the 1-D dimensionless coordinate starting at the fixed-temperature boundary. (Note that the similarity solution is independent of the scaling of I in x_d and t_d, but the superposed solutions is dependent on such a scaling. A reflected front is a leading edge of diffusion that encounters a no-flow boundary and stops propagating in that direction and reflects backward.) The solution for cylinders that is obtained using the asymptotic expansion of the Bessel functions is complicated. The temperature solutions for slab-like, spherical, and cylindrical blocks are, respectively:

$$T_d = \sum_{n=1}^{\infty} (-1)^{n-1} \left[\text{erfc}\frac{(2n-1)-x_d}{2\sqrt{t_d}} + \text{erfc}\frac{(2n-1)+x_d}{2\sqrt{t_d}} \right], \quad (5a)$$

$$T_d = \frac{1}{x_d} \sum_{n=1}^{\infty} \left[\text{erfc}\frac{(2n-1)-x_d}{2\sqrt{t_d}} - \text{erfc}\frac{(2n-1)+x_d}{2\sqrt{t_d}} \right], \quad (5b)$$

$$T_d = \frac{1}{x_d^{1/2}} \text{erfc}\frac{1-x_d}{2\sqrt{t_d}} + \frac{(1-x_d)\sqrt{t_d}}{4x_d^{3/2}} \text{ierfc}\left(\frac{1-x_d}{2\sqrt{t_d}}\right) + \frac{(9-7x_d^2-2x_d)t_d}{32x_d^{5/2}} \text{i}^2\text{erfc}\left(\frac{1-x_d}{2\sqrt{t_d}}\right) \ldots, \quad (5c)$$

where ierfc() is the integral error function (Crank, 1975, p. 200). Note that equation (5c), does not contain terms corresponding to multiple reflections (Carslaw & Jaeger, 1959, p. 330). The solutions at the center ($x_d = 0$) of spherical and cylindrical blocks are, respectively, written

$$T_d = \frac{1}{\sqrt{\pi t_d}} \sum_{n=1}^{\infty} \exp\left[-\frac{(2n-1)^2}{4t_d} \right], \quad (5d)$$

$$T_d = \frac{1}{\sqrt{\pi t_d}} \exp\left(-\frac{1}{8t_d}\right) K_{1/4}\left(\frac{1}{8t_d}\right) + \cdots, \quad (5e)$$

where $K_{1/4}(\ )$ is the modified Bessel function of the second kind of a positive order of ¼.

The exponential-series solutions in equation (4) converge satisfactorily for moderate and large t_d, while the error-function-series solutions in equation (5) converge quite rapidly for all except large t_d. Based on the complementary convergence behaviors of these two types of solutions, we proposed combining the early-time solutions based on equation (5) and the late-time solutions based on equation (4) that are continuous at the switchover dimensionless time for temperature (t_{d0}^T). t_{d0}^T of the time partitioning is determined to minimize the maximum approximation errors throughout the entire time domain, as shown below.

The unified-form combined temperature solutions for slabs, spheres, and cylinders can be written

$$T_d = \begin{cases} \dfrac{1}{x_d^{\frac{p-1}{2}}} \displaystyle\sum_{j=1}^{N^T} \left[c_{1j} \operatorname{erfc} \dfrac{(2j-1)-x_d}{2\sqrt{t_d}} + c_{2j} \operatorname{erfc} \dfrac{(2j-1)+x_d}{2\sqrt{t_d}} \right], \; t_d < t_{d0}^T, & \text{(6a)} \\ 1 - \displaystyle\sum_{j=1}^{N^T} b_{1j}^T \exp\left[-b_{2j}^T t_d \right] X\left(\sqrt{b_{2j}^T} x_d \right), \; t_d \geq t_{d0}^T & \text{(6b)} \end{cases}$$

where c_{1j} and c_{2j} are the sign parameters for the two error functions, respectively, determined by comparing with equation (5), b_{1j}^T and b_{2j}^T are the capacity ratios and rate coefficients of the late-time temperature solutions, $X()$ is the separated spatial solution in terms of x_d, and N^T is the number of the leading terms used for both the early and late-time solutions. For cylinders, the early-time solution is represented by the first three terms in equation (5c) with $N^T=1$.

Convergence behavior of both types of solutions and the combined solutions for slabs, spheres, and cylinders are presented in Figure 1. For slabs and spheres, the error-function-series solution with $N=10$ (the first 10 terms) and the exponential-series solution with $N=10,000$ produce the exact solution over the time domain $t_d=[10^{-7}, 10]$. For slabs, for example, the error-function-series solution with $N=1$ is the exact solution (acting like in a semi-infinite domain without reflections) until the temperature front reaches the point of interest. The arrival time at the block center with $T_d=1.15\times10^{-6}$ is $t_d=0.02$. The solution with multiple reflections with $N=2, 3, 4, 5, 6$ produces the same accuracy at the block center at $t_d=0.18, 0.50, 0.98, 1.62, 2.42$, respectively. Indeed, at $t_d=2.42$ with $N=6$, $T_d=0.99675$ with seven digits of significance. This indicates the error-function-series solutions converge rapidly at small and moderate t_d. The exponential-series solution with $N=1$ is also exact for $t_d \geq 0.8041$ with seven digits of significance. This indicates that this type of solution is suitable for investigating the late-time behavior of back-diffusion in contaminant transport with high accuracy (e.g., Haggerty et al., 2000, 2004). Similar behavior of convergence is observed for spheres (see Figures 1c and 1d). For cylinders (see Figures 1e and 1f), only the normal-accuracy approximation is shown because the exact error-function-series solution is not available.

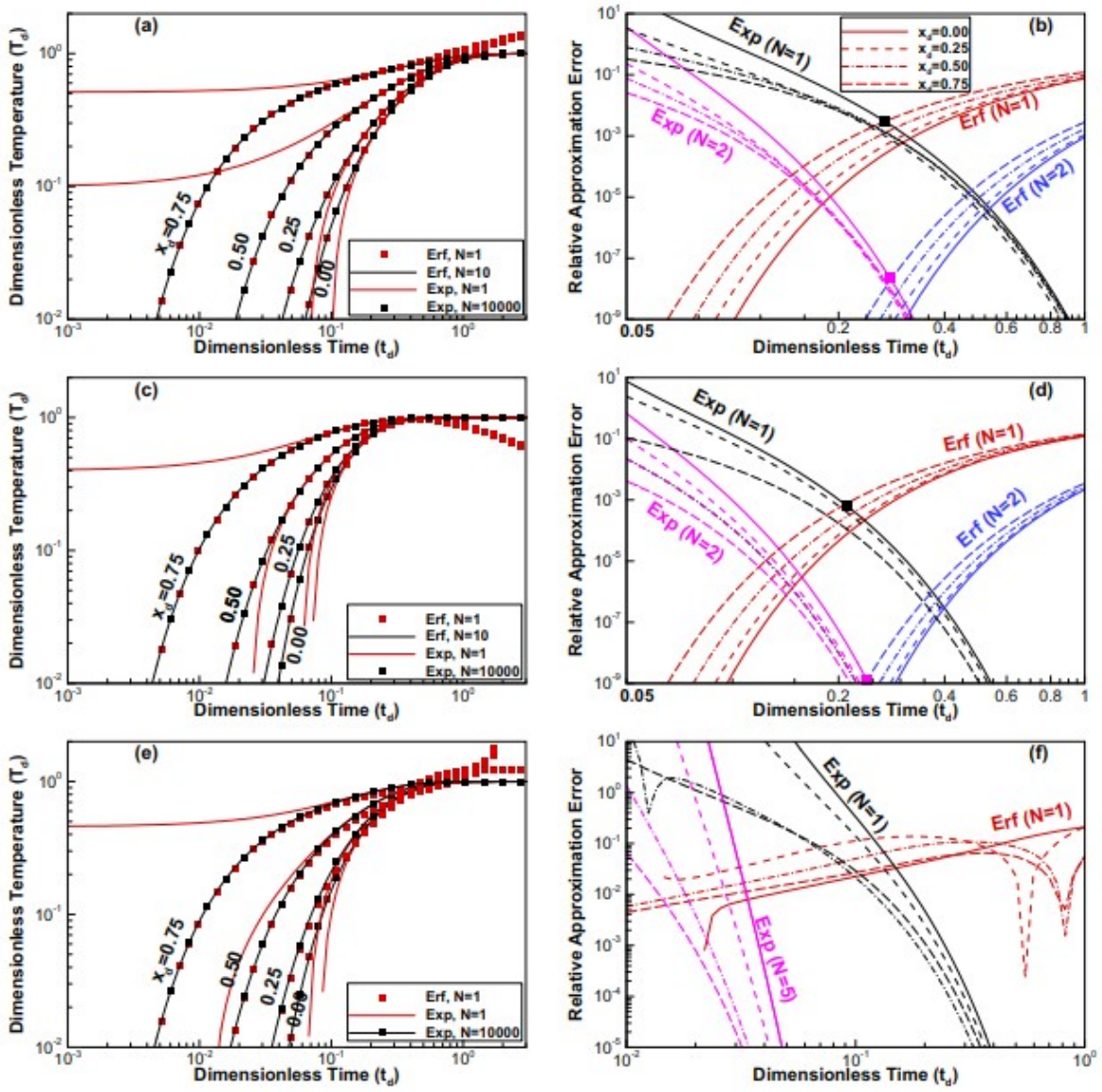

Figure 1

Comparison of (left plots) convergence between the error-function-series and the exponential-series solutions with different terms of both series, and (right plots) relative approximation errors of these two solutions and the combined solutions with $N=1$ and 2 (relative to the exact solutions calculated using the exponential series with $N=10,000$) for (a) and (b) slab-like, (c) and (d) spherical, and (e) and (f) cylindrical blocks. In all subplots, $x_d=0.0,\ 0.25,\ 0.50,\ 0.75$. The symbols in Figures 1b and 1d denote the relative approximation errors at the switchover dimensionless times.

For the combined solution for slabs, in the case of $N^T=1$ (i.e., the leading term in the early and late-time solutions), the maximum approximation errors in percent are 0.304, 0.102, 0.139, and 0.294 at $x_d=0.0,\ 0.25,\ 0.50,\ 0.75$, respectively, for $t_{d0}^T=0.27$ that is selected to minimize the maximum relative approximation errors (see Figure 1b). The same t_{d0}^T is used for all x_d values, as t_{d0}^T varies only slightly from 0.25 to 0.32 for $x_d=[0.0,\ 0.75]$. This accuracy is sufficient for all applications of heat transfer in the subsurface. When a higher accuracy is needed, $N^T=2$ can lead to relative approximation errors less than 0.22×10^{-7} with

$t_{d0}^{T}=0.28$. This rapid and uniform convergence behavior of the combined solution can be attributed to the rapid convergence of the two types of solutions in their respective time regimes. A similar convergence behavior of the combined solution for spheres is also observed in Figure 1d, with $t_{d0}^{T}=0.21$ for $N^{T}=1$ and 0.24 for $N^{T}=2$.

The switchover dimensionless time is 0.27 and 0.28 for slabs and 0.21 and 0.24 for spheres for the normal and high-accuracy approximations with $N^{T}=1$ and 2, respectively. These t_{d0}^{T} values are determined to minimize the maximum approximation errors using both early and late-time solutions. Heisler (1947) used $t_{d0}^{T}=0.2$ to control approximation errors less than 1% for slabs, spheres, and cylinders. Only the leading term in equation 4a was used to derive the late-time solution for $t_d \geq 0.2$ and plot the results in the classic Heisler charts (Hahn & Ozisik, 2012; Holman, 1990), while the solution for $t_d < 0.2$ was obtained by a means of an electrical analogy, rather than the error-function-series solutions in equation (5). A dimensionless time of 0.05 was used to partition the time interval of integration for Green's functions into short and long-time subintervals where the Green's functions were approximated by their small and large-time representations; the time-partitioning method can have at least eight digit accuracy for the short-time Green's functions (Beck et al., 2004, 2006; McMasters et al., 2002; Yen et al., 2002). This method was developed to integrate the very fundamental Green's functions of point source to account for various boundary conditions and internal heat generation. Our time-partitioning method is significantly simpler and takes advantage of the fast convergence of the existing two types of solutions in their respective time regimes; the normal and high-accuracy approximation can be easily achieved using $N^{T}=1$ and 2, respectively, with uniform convergence clearly demonstrated in Figure 1.

2.2 Temperature Solutions for 2-D and 3-D Rectangular Blocks

For 3-D rectangular parallelepipeds with three coordinates $x_i\ (i=1, 2, 3)$, we introduce the half-widths l_i, the aspect ratios R_{li}, and the dimensionless area-to-volume ratio R:

$$l=l_1 \leq l_2 \leq l_3,\ R_{li}=l/l_i,\ R=Al/V, \quad (7a)$$

where A, V, and l are the boundary area, volume, and minimum half-width of the blocks. We introduce the dimensionless spatial variables and the dimensionless times

$$x_{di}=x_i/l_i,\ t_{di}=Dt/l_i^2=R_{li}^2 t_d. \quad (7b)$$

Note that $t_d=Dt/l^2$ is always written in terms of the minimum half-width. The same definitions hold for 2-D rectangular blocks.

It is well-known that the temperature solution for a 1-D slab, a 2-D rectangle, and a 3-D rectangular parallelepiped can be written in a generalized product form (e.g., Crank, 1975, p. 25)

$$T_d = 1 - \prod_{i=1}^{N_d} T'_{di}(x_{di}, t_{di}), \quad (8a)$$

where N_d is the dimensionality of the blocks ($=1$ for slabs, $=2$ for rectangles, $=3$ for rectangular parallelepipeds), and $T'_{di}(x_{di}, t_{di})$ is the 1-D slab temperature solution for the case with a unit initial temperature and zero boundary temperature, which is complementary to the solution in equations 4a or (5a) in the form $T'_{di}(x_{di}, t_{di}) = 1 - T_{di}(x_{di}, t_{di})$.

For numerical evaluation, we first consider the 1-D slab complementary solution in each direction independently, and then calculate the early and late-time solutions in that direction using the time partitioning with its own dimensionless time (t_{di}) and the same switchover dimensionless time t_{d0}^T for slabs as follows:

$$T'_{di}(x_{di}, t_{di}) = \begin{cases} 1 - \sum_{n_i=1}^{N^T} (-1)^{n_i - 1} \left[\operatorname{erfc} \frac{(2n_i - 1) - x_{di}}{2\sqrt{t_{di}}} + \operatorname{erfc} \frac{(2n_i - 1) + x_{di}}{2\sqrt{t_{di}}} \right], \; t_{di} < t_{d0}^T, & (8b) \\ \sum_{n_i=1}^{N^T} \frac{4(-1)^{n_i - 1}}{(2n_i - 1)\pi} \exp\left[-\left(\frac{2n_i - 1}{2} \right)^2 \pi^2 t_{di} \right] \cos\left(\frac{2n_i - 1}{2} \pi x_{di} \right), \; t_{di} \geq t_{d0}^T. & (8c) \end{cases}$$

We finally perform the multiplication of the calculated solutions for all the directions using (8a).

In equation (8), we can minimize the number of leading terms and use $N^T = 1$ or 2 for both the early and late-time solutions in each direction. A uniform convergence is achieved, with $N^T = 1$ for normal-accuracy and $N^T = 2$ for high-accuracy approximations, in the entire time domain, as well as in the multidimensions. Note that the first type of exponential-series solution contains equations 8a and (8c) while the second type of error-function-series solution contains equations 8a and (8b), both for $N^T = \infty$ and the entire time domain without time partitioning.

As shown in Figures 2a and 2d, the convergence of equation (8a) with the complementary error-function-series slab solution in equation (8b) alone is rapid for the entire time domain as $N = 10$ is sufficient to reproduce the exact solutions for a rectangle with $R_{l2} = 0.5$ and a rectangular parallelepiped with $R_{l2} = 0.5$ and $R_{l3} = 0.2$. The convergence of equation (8a) with the complementary trigonometric-exponential-series solution in equation (8c) alone is very slow as $N = 10,000$ is needed for the time range $t_d = [10^{-7}, 10]$. As shown in Figures 2b and 2e, the leading term and the first two terms of these two types of solutions in equations (8b) or (8c) for both example blocks produce less accurate approximations than for the 1-D slab (see Figure 1b). This disparity becomes worse for strongly anisotropic blocks with a smaller R_{li} and a higher dimension. For both example blocks, the convergence of equation 8a with the combined complementary solutions is rapid and uniform as only $N^T = 1$ or 2 is needed to achieve relative approximation errors less than 0.003 or 10^{-7}(see Figures 2c and 2f). Again $t_{d0}^T = 0.27$ is used for $N^T = 1$ and $t_{d0}^T = 0.28$ is used for $N^T = 2$ for the slab in each direction. This convergence behavior of 2-D and 3-D

rectangular blocks is very similar to that of 1-D slab (see Figure 1b), indicating that there is no loss of convergence speed and approximation accuracy by the higher dimension. This rapid and uniform convergence for 2-D/3-D rectangular blocks can be attributed to the time partitioning between the early and late-time solutions using (t_{di}, t_{d0}^{L}) in each direction to avoid the effect of block anisotropy.

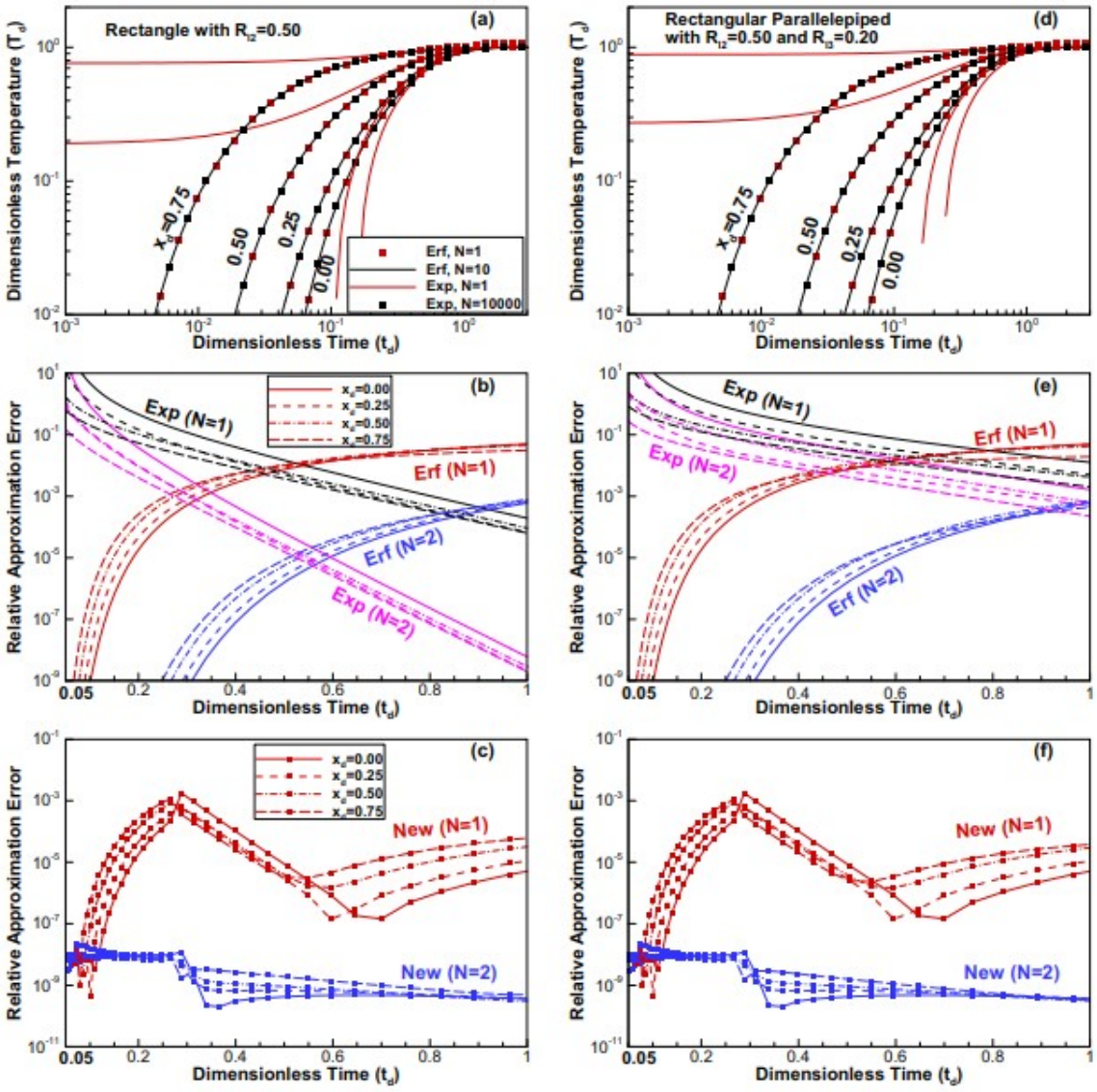

Figure 2

Convergence of (first row) the exact solutions with the error-function-series and the exponential-series, and (second row) the relative approximation errors of both series and of the combined solution with uniform convergence (third row) with the leading term ($N=1$) and the first two terms ($N=2$) for both a rectangle with (left) $R_{i2}=0.5$ and a rectangular parallelepiped with (right) $R_{i2}=0.5$ and $R_{i3}=0.2$.

The advantage of the combined solution in equation 8a is demonstrated by comparing to the alternative solution using the time partitioning, with (t_{d}, t_{d0}^{L}), between the early-time or the late-time solution for all directions:

$$T_d=\begin{cases}1-\prod_{i=1}^{N_d}\left\{1-\sum_{n_i=1}^{N_i^{Te}}(-1)^{n_i-1}\left[\operatorname{erfc}\dfrac{(2n_i-1)-x_{di}}{2R_{li}\sqrt{t_d}}+\operatorname{erfc}\dfrac{(2n_i-1)+x_{di}}{2R_{li}\sqrt{t_d}}\right]\right\}, & t_d<t_{d0}^{T}, \quad (9a)\\ 1-\prod_{i=1}^{N_d}\sum_{n_i=1}^{N_i^{Tl}}\dfrac{4(-1)^{n_i-1}}{(2n_i-1)\pi}\exp\left[-\left(\dfrac{2n_i-1}{2}\right)^2\pi^2R_{li}^2t_d\right]\cos\left(\dfrac{2n_i-1}{2}\pi x_{di}\right), & t_d\geq t_{d0}^{T} \quad (9b)\end{cases}$$

where N_i^{Te} and N_i^{Tl} are the number of leading terms for the ith direction that are kept for the early and late-time solutions, respectively. Following the specific arrangement of the x_i directions, we have $N_1^{Te}\geq N_2^{Te}\geq N_3^{Te}$; this means $N_1^{Te}=1, 2$ may be sufficient for normal and high-accuracy approximations for 2-D and 3-D rectangular blocks. For the late-time solutions, we have $N_1^{Tl}\leq N_2^{Tl}\leq N_3^{Tl}$ because of the effect of R_{li}^2 on the exponentials in equation (9b). The convergence pattern of equation (9b) is highly irregular for strongly anisotropic rectangular blocks with $R_{li}\ll 1$. For example, for a rectangle with $R_{l2}=0.1$, $t_{d2}=0.01t_d$; at $t_{d1}=0.27$ for the x_1 direction, we have $t_{d2}=0.0027$ at which the early-time solution is extremely accurate with $N_2^{Te}=1$, but the late-time solution has a relative approximation error of 0.21% at the block center even using $N_2^{Tl}=100$. This convergence irregularity is caused by the irregular time partitioning at $t_{d3}\leq t_{d2}\leq t_{d1}=t_{d0}^{T}$, and decreases with the reduction in block anisotropy. Only for squares and cubes, $N_1^{Te}=N_2^{Te}=N_3^{Te}=N_1^{Tl}=N_2^{Tl}=N_3^{Tl}$, and the alternative solution is identical to the combined solution in equation (8), with a uniform convergence.

3 Fundamental Cumulative and Transient Heat Flux Equations

For many applications of heat transfer, we may not be interested in the temperature distribution inside a block, but only interested in the heat flux through the boundary of the block. This heat flux can be considered as a sink or source to large-scale heat advection and dispersion through fracture networks, for example. Zhou et al. (2017) developed the unified-form flux solutions, with normal-accuracy approximations, for 1-D isotropic blocks (slabs, spheres, cylinders) by combining their two types of leading-term solutions with time partitioning. They extended the unified-form solutions to 2-D/3-D rectangular blocks by fitting the early-time solution (i.e., a three-term polynomial in terms of $\sqrt{t_d}$) using the exact exponential-type solutions for many combinations of aspect ratios.

In this section, we first focus on both normal and high-accuracy flux solutions for 1-D slab-like and 2-D/3-D rectangular blocks, using the product of the combined 1-D slab solutions with the time partitioning based on (t_{di}, t_{d0}) in each direction, where t_{d0} is the switchover dimensionless time for heat flux. This product form of flux solutions is useful in calculating the cumulative and transient flux because the rapid and uniform convergence is achieved regardless of the degree of block anisotropy. We then derive new early-time solutions for 2-D/3-D rectangular blocks, with solution coefficients linked to dimensionless area-to-volume ratio and aspect ratios. The second, nonproduct form of first-order heat flux equations with these early-time solutions and late-time exponential solutions, using the time partitioning

based on (t_d, t_{d0}), can be easily used to couple large-scale heat advection and dispersion. Both the dimensionless cumulative flux equations and the transient flux equations are presented.

3.1 Flux Equations With Rapid and Uniform Convergence

Similarly, for 1-D/2-D/3-D temperature solutions, the cumulative flux for 1-D slab-like and 2-D/3-D rectangular blocks can be written as a product of the complementary flux (M'_{di}) of 1-D slabs in the different directions. The two types of standard solutions can be written, respectively, in a generalized product form:

$$M_d = 1 - \prod_{i=1}^{N_d} M'_{di}(t_{di}), \quad (10a)$$

$$M'_{di}(t_{di}) = \frac{2}{\pi^2} \sum_{n_i=1}^{\infty} \left(\frac{2}{2n_i-1}\right)^2 \exp\left[-\left(\frac{2n_i-1}{2}\right)^2 \pi^2 t_{di}\right], \quad (10b)$$

$$M'_{di}(t_{di}) = 1 - \left[\frac{2}{\sqrt{\pi}}\sqrt{t_{di}} + 4\sqrt{t_{di}} \sum_{n_i=1}^{\infty} (-1)^{n_i} \text{ierfc}\left(n_i/\sqrt{t_{di}}\right)\right], \quad (10c)$$

Note that $M_{di}(t_{di}) = 1 - M'_{di}(t_{di})$ shows the complementary relationship between the case with unit boundary temperature and zero initial temperature and the complementary case with zero boundary temperature and unit initial temperature.

The unified-form flux equations for 1-D/2-D/3-D blocks can be written with the combined complementary flux solutions:

$$M_d = 1 - \prod_{i=1}^{N_d} M'_{di}(t_{di}), \quad (11a)$$

$$M'_{di}(t_{di}) = \begin{cases} 1 - \left[\frac{2}{\sqrt{\pi}}\sqrt{t_{di}} + 4\sqrt{t_{di}} \sum_{n_i=1}^{N-1} (-1)^{n_i} \text{ierfc}\left(n_i/\sqrt{t_{di}}\right)\right], & t_{di} < t_{d0}, \quad (11b) \\ \frac{2}{\pi^2} \sum_{n_i=1}^{N} \left(\frac{2}{2n_i-1}\right)^2 \exp\left[-\left(\frac{2n_i-1}{2}\right)^2 \pi^2 t_{di}\right], & t_{di} \geq t_{d0}. \quad (11c) \end{cases}$$

The switchover dimensionless time for slabs can be determined by comparing equations 5a and 10c to the semi-infinite solution, $M_d = \frac{2}{\sqrt{\pi}}\sqrt{t_d}$.

The effect of the central no-flow boundary at $x_d = 0$ on the flux is negligible for $t_d < t_{d0}$ for slabs. Indeed, $t_{d0} = 0.213$ is the arrival time of the temperature front (reflected by the no-flow boundary) back to the constant-temperature boundary at $x_d = 1$, with a temperature of 0.0022. This means that before the reflected front arrives at the constant-temperature boundary, the slab flux solutions are equal to the semi-infinite ones. At $t_{d0} = 0.213$, the approximation error is less than 0.153%.

As shown in Figures 3a and 3b for slabs, the convergence of the exponential-series solution by equations 10a and 10b and of the error-function-series solution by equations 10a and 10c is not satisfactory for the early times and

the late times, respectively. The maximum approximation error of the combined solution with equation (11) is 0.15%, when $N=1$ is used with $t_{d0}=0.213$ (Zhou et al., 2017). For the high-accuracy approximation with $N=2$, the first integral-error-function term on the right-hand side of equation (11b), which is the contributions from the first reflection, is needed as well as one additional exponential term in equation (11c). The switchover dimensionless time for slabs with $N=2$ is determined to be 0.254 and the maximum relative approximation error is reduced dramatically to less than 10^{-8}. This fast and uniform convergence of the combined solution is clearly shown in Figure 3b, along with the irregular convergence of the two types of fundamental solutions.

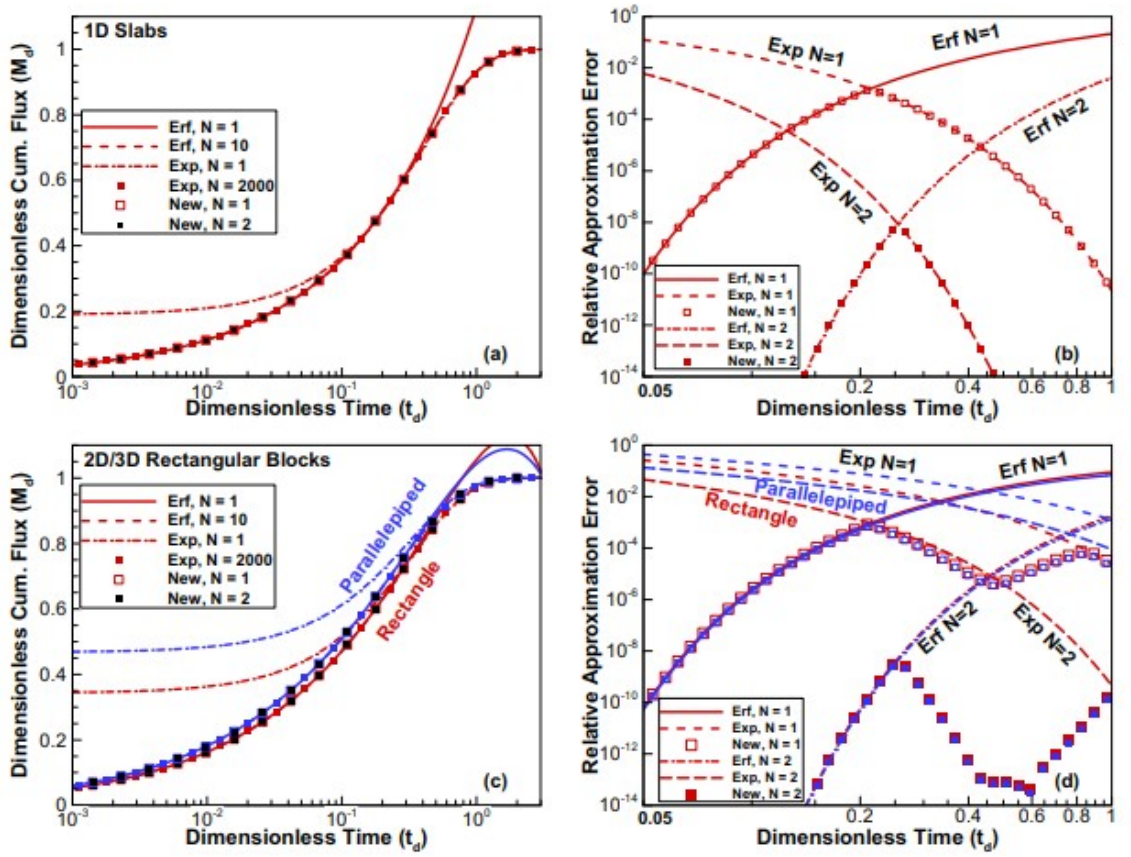

Figure 3

(left) Comparison of the convergence and (right) relative approximation errors of the error-function-series, exponential-series, and combined solutions for heat flux with different terms (N) for (a) and (b) 1-D slab and (c) and (d) 2-D/3-D rectangular blocks (a rectangle with $R_{l2}=0.5$ in red lines and symbols and a rectangular parallelepiped with $R_{l2}=0.5$, $R_{l3}=0.2$ in blue lines and symbols).

Figures 3c and 3d show the convergence and the relative approximation error of the error-function-series, exponential-series, and combined solutions for a rectangle with $R_{l2}=0.5$ and a rectangular parallelepiped with $R_{l2}=0.5$ and $R_{l3}=0.2$. The error-function-series solution with $N=10$ and the exponential-series solution with $N=2,000$ in each direction are needed to reproduce the exact

solutions over $t_d=[10^{-7}, 10]$. With $N=1$ or 2, the relative error of the error-function-series solutions slightly decreases from slab, while that of the exponential-series solutions increases dramatically for the two example blocks because of the block anisotropy. The relative error of the combined solutions is less than 0.001 for both blocks with $N=1$ and $t_{d0}=0.213$, and less than 5.0×10^{-9} with $N=2$ and $t_{d0}=0.254$. These relative errors are even smaller than those (0.0015 and 9.0×10^{-9}) for slabs. Note that the first peak in the relative approximation errors of the combined solutions for each example block at $t_d=0.213$ for $N=1$ and 0.254 for $N=2$ corresponds to the highest relative errors at the partitioning times in the x_1 direction; the second peak at $t_d=0.852$ for $N=1$ and 1.016 for $N=2$ corresponds to the partitioning times in the x_2 direction.

The fast and uniform convergence of the developed flux equations in equation 11a is achieved using $N=1$ for the first-order normal-accuracy approximations and $N=2$ for the high-accuracy approximations, regardless of the degree of block anisotropy. This convergence behavior can be attributed to the time partitioning between the early and late-time solutions in the ith direction that is based on the comparison between t_{di} and t_{d0} for slabs. Note that the upper limits of the summation for the integral-error-function terms in equation (11b) and for the exponentials in equation (11c) are $N-1$ and N, respectively.

Based on the cumulative flux equations in equation (11) with $N=1$, we can obtain the first-order, dimensionless transient heat flux of a single unit-volume block, f_d, per unit temperature change at its boundary written:

$$f_d=\frac{dM_d}{dt_d}=-\sum_{i=1}^{N_d}\left\{R_{fi}^2\frac{dM'_{di}}{dt_{di}}\prod_{j=1,j\neq i}^{N_d}M'_{dj}(t_{dj})\right\}, \quad (12a)$$

$$-\frac{dM'_{di}}{dt_{di}}=\begin{cases}\dfrac{1}{\sqrt{\pi}\sqrt{t_{di}}}, & t_{di}<t_{d0} \quad (12b)\\ 2\exp\left[-\dfrac{\pi^2}{4}t_{di}\right], & t_{di}\geq t_{d0}. \quad (12c)\end{cases}$$

The first, product form of flux equations, equations (11) and (12), are very efficient for numerical calculations because of rapid and uniform convergence with $N=1$ or 2. However, they may not be convenient for coupling with global heat advection and dispersion in fracture networks because the Laplace transforms of equation (12) is complicated.

3.2 Flux Equations With Physical Insights

The second, nonproduct form of flux equations has the unified-form solutions for isotropic and anisotropic blocks (Zhou et al., 2017):

$$M_d=\begin{cases}a_1t_d^{1/2}+a_2t_d+a_3t_d^{3/2}+O(ierfc), & t_d<t_{d0} \quad (13a)\\ 1-\sum_{j=1}^{N}b_{1j}\exp\left(-b_{2j}t_d\right), & t_d\geq t_{d0}, \quad (13b)\end{cases}$$

where a_1, a_2, a_3, b_1, and b_2 are the first-order solution coefficients, $O(\text{ierfc})$ are the higher-order terms that represent multiple reflections, and N is the number of truncated exponential terms in equations 10a and 10b. The same time-partitioning method with a switchover time has been used by others (e.g., Dykhuizen, 1990; Heisler, 1947; March et al., 2016; Zhang et al., 2011) to take advantage of the satisfactory convergence of different solutions in their respective time regimes.

For rectangles and rectangular parallelepipeds, the first-type, exponential-series flux solutions (Carslaw & Jaeger, 1959; Crank, 1975; Lim & Aziz, 1995; Zhou et al., 2017) can be written in terms of dimensionless time t_d:

$$M_d=1-\prod_{i=1}^{N_d}\left\{\frac{8}{\pi^2}\sum_{n_i=1}^{\infty}\frac{1}{(2n_i-1)^2}\exp\left[-(2n_i-1)^2R_{li}^2\frac{\pi^2}{4}t_d\right]\right\}. \quad (14)$$

The convergence of this exponential-series solutions is only satisfactory for moderate and large t_d and is affected by block anisotropy with small R_{li}.

The second-type, error-function-series flux solutions for rectangles and rectangular parallelepipeds for small and moderate t_d are not available in the literature. We derive these solutions using the error-function temperature solutions for 1-D slabs (see Appendix Appendix A), which are written, respectively:

$$M_d=\frac{2}{\sqrt{\pi}}(1+R_{l2})t_d^{1/2}-\frac{4}{\pi}R_{l2}t_d+\cdots \quad (15a)$$

$$M_d=\frac{2}{\sqrt{\pi}}(1+R_{l2}+R_{l3})t_d^{1/2}-\frac{4}{\pi}(R_{l2}+R_{l3}+R_{l2}R_{l3})t_d+\frac{8}{\pi^{3/2}}(R_{l2}R_{l3})t_d^{3/2}+\cdots. \quad (15b)$$

Note that only the leading error-function term in equation (8b) is used to simplify the derivation of equation (15). Unlike equation 14, these solutions are valid only for small to moderate t_d.

As shown by the two types of flux solutions in equations 14 and (15), the unified-form cumulative flux equations, equation (13), can still hold for 2-D and 3-D rectangular blocks, without the higher-order terms. By comparison, the first-order solution coefficients of both the early-time and the late-time solutions in equation (13) for a 2-D rectangular block can be written:

$$a_1=2(1+R_{l2})/\sqrt{\pi},\ a_2=-4R_{l2}/\pi,\ a_3=0, \quad (16a)$$

$$b_{1j}=\left(\frac{8}{\pi^2}\right)^2\Big/\left[(2n_{1j}-1)^2(2n_{2j}-1)^2\right], \quad (16b)$$

$$b_{2j}=\frac{\pi^2}{4}c_j;\ c_j=(2n_{1j}-1)^2+(2n_{2j}-1)^2R_{l2}^2. \quad (16c)$$

Note that Zhou et al. (2017) obtained equation (16a) with $a_2=-1.2735R_{l2}$ by fitting equation (13a) for a_2 to the exact exponential-series solutions in equation 14, calculated using the first $2,000\times2,000$ terms, with different values

of aspect ratio $R_{l2}=[0,\ 1]$. Both the mathematical derivation and the solution fitting produce almost identical results for a_2.

The solution coefficients for a rectangular parallelepiped can be written:

$$a_1=2(1+R_{l2}+R_{l3})/\sqrt{\pi},\ \ a_2=-4(R_{l2}+R_{l3}+R_{l2}R_{l3})/\pi,\ a_3=8R_{l2}R_{l3}/\pi^{3/2},\quad(17a)$$

$$b_{1j}=\left(\frac{8}{\pi^2}\right)^3\Big/\left[(2n_{1j}-1)^2(2n_{2j}-1)^2(2n_{3j}-1)^2\right],\quad(17b)$$

$$b_{2j}=\frac{\pi^2}{4}c_j;\ c_j=(2n_{1j}-1)^2+(2n_{2j}-1)^2R_{l2}^2+(2n_{3j}-1)^2R_{l3}^2.\quad(17c)$$

Note that Zhou et al. (2017) obtained equation (17a) with $a_2=-1.2735R_{l2}-1.2645R_{l3}-1.2791R_{l2}R_{l3}$ and $a_3=1.4232R_{l2}R_{l3}$ by fitting equation (13a) for a_2 and a_3 to the exact exponential-series solutions in equation 14, calculated using the first $1,000\times1,000\times1,000$ terms, with different values of aspect ratio pair ($R_{l2},\ R_{l3}$). Again, both methods produce very close a_2 and a_3 with the same forms of correlations with the aspect ratios.

For both 2-D and 3-D rectangular blocks, the number of exponential terms (N) needed for the late-time solutions in equation (13b) can be determined practically using

$$c_j\le 11\ \text{ with }\ b_{1j}\exp\left(-b_{2j}t_{d0}\right)\ge tol,\quad(18)$$

where tol is a cutoff, depending on the degree of anisotropy. For example, $tol=5\times10^{-4}$ for $R_{l2}>0.1$, while $tol=1\times10^{-4}$ is needed for $R_{l2}\le0.1$ to control the relative error below 0.5% for a rectangle with $R_{l2}=0$. $N=39$ is needed for highly anisotropic rectangles with $R_{l2}<0.01$, and $N=59$ is needed for a highly anisotropic rectangular parallelepiped with $R_{l2}<0.01$ or $R_{l3}<0.01$. On the other hand, $N=1$ is needed for squares and cubes. The switchover dimensionless time for flux for slabs, squares, and cubes is 0.213, 0.215, and 0.229, respectively, while that for both rectangles and rectangular parallelepipeds is 0.22 (see Table 1 in Zhou et al., (2017)).

The second, nonproduct form of dimensionless transient heat flux can be written from equation (13):

$$f_d=\frac{dM_d}{dt_d}=\begin{cases}a_1/(2\sqrt{t_d})+a_2+\dfrac{3}{2}a_3\sqrt{t_d},\ t_d<t_{d0}\\[2ex]\sum_{j=1}^{N}b_{1j}b_{2j}\exp\left(-b_{2j}t_d\right),\ t_d\ge t_{d0}\end{cases}.\quad(19)$$

Regarding the physical meaning of the coefficient a_1, we note that as derived in Appendix Appendix A, $a_1\sqrt{t_d}$ represents the cumulative heat flux assuming the entire block surface acts like a semi-infinite block without interference at block corners. $a_1(=2R/\sqrt{\pi})$ depends only on the dimensionless area-to-volume ratio (R), which is 1, $(1+R_{l2})$, and $(1+R_{l2}+R_{l3})$ for a slab, a rectangle, and a rectangular parallelepiped, respectively. For a rectangle, the interference accounts for $-4R_{l2}t_d/\pi$ in the cumulative heat flux, i.e., a time-constant heat flux of $-4R_{l2}/\pi$ that is negligible at a very small t_d in comparison with the $0.5a_1/\sqrt{t_d}$

. For 1-D slab-like and 2-D/3-D rectangular blocks, the first term in equation (13a) is dominant at very early time (e.g., $t_d \leq 0.001$). The measured early cumulative heat flux can be used to estimate coefficient a_1 for the dimensionless area-to-volume ratio, and contains information on the dimensionality (e.g., $R=1, 2, 3$ for slab, square, and cube) of the block. Theoretically, the entire profile of M_d with respect to t_d has to be used to estimate heat transfer area per unit volume of fractured rock and the aspect ratios, as well as the block dimensionality and anisotropy.

In the second, nonproduct form of flux equations, equations (13) and 19, the convergence of the late-time solution is irregular for highly anisotropic blocks and truncated exponentials with $N > 1$ are needed. However, the physical insights are provided by linking the coefficients of the early-time solution to the dimensionless area-to-volume ratio and aspect ratios, and by linking the rate coefficients in the late-time solutions to the aspect ratios. This form of flux equations is useful in (1) inverse modeling to estimate the dimensions, aspect ratios, and heat transfer area of the blocks, and (2) coupling local heat conduction in blocks with global heat advection and dispersion through high-permeability channels or fractures.

3.3 Multirate Heat Flux

For a representative porous-medium mass that consists of *k* blocks of different shapes and different sizes, with a minimum half-width l^i and volume fraction $w^i, i=1, 2, \ldots, k$, we can write the dimensionless cumulative heat flux, similar to the single-block case, as

$$M_d = \sum_{i=1}^{k} w^i M_d^i;\ t_d^i = Dt/(l^i)^2. \quad (20a)$$

Let us examine the fracture-matrix heat flux, F, per unit volume of water-saturated fractured media with fracture volumetric fraction ϕ_f and matrix fraction $1-\phi_f$. It is assumed that the *k* blocks of different shapes and different sizes also have different intrinsic porosity ϕ_m^i and thermal diffusivity D^i. The total heat stored in these matrix blocks per unit volume of fractured media at time *t* is

$$W(t) = (1-\phi_f) \sum_{i=1}^{k} w^i H^i (T_1 - T_0) M_d^i \quad (20b)$$

and

$$H^i = (1-\phi_m^i)\rho_g c_g + \phi_m^i \rho_w c_w, \quad (20c)$$

where H is the internal heat, ρ is the density, c is the specific heat, and subscripts g and w denote the grain and water, respectively.

The heat flux between surrounding fractures and these blocks per unit volume of fractured media is written

$$F(t)=\frac{dW}{dt}=(1-\phi_f)\sum_{i=1}^{k} w^i H^i (T_1-T_0) f_d^i \frac{D^i}{(l^i)^2}. \quad (20d)$$

4 Examples of Numerical Evaluation

4.1 Temperature Solutions

Here the approximate solutions in equations (6) and (8) developed above with time partitioning are used for the numerical evaluations of temperature distributions in a slab, a sphere, and a cylinder, and in rectangles and rectangular parallelepipeds with different aspect ratios (including a square and a cube), respectively. The three aspect ratios for rectangles are $R_{l2}=1.0,\ 0.5,\ 0.2$, while the three pairs of aspect ratios for rectangular parallelepipeds are $(R_{l2}, R_{l3})=(1.0, 1.0),\ (0.5, 0.2),$ and $(0.2, 0.1)$. The grids for calculating dimensionless temperature have 201 logarithmically spaced dimensionless times in the range $t_d=[10^{-6}, 10]$ and 201 linearly spaced spatial variables $x_{di}=[0, 1]$.

Figure 4 shows the contours of dimensionless temperature calculated using the developed approximate solutions with $N=2$ and high accuracy for the isotropic blocks over the time and space domains, and rectangular blocks over the spatial domain at three selected times ($t_d=0.02,\ 0.2,$ and 0.5). As shown in Figures 4a–4c, the developed approximate solutions can capture the dimensionless temperature for $t_d=[10^{-6}, 10]$ and the arrival times at the block center and various locations. For example, the arrival time of $T_d=0.0001$ at the slab center is $t_d=0.032$. Figures 4d–4f show the contours of dimensionless temperature at three different times for three rectangles with $R_{l2}=1.0,\ 0.5,$ and 0.2, respectively. At $t_d=0.02$, the profile of T_d from the fixed-temperature boundary to the temperature front looks like that for a slab, except at the rectangular corner. At later time, the temperature over the entire domain is affected by the temperature profiles in different directions. The highly anisotropic rectangle with $R_{l2}=0.2$ acts like a slab more than the isotropic square. Clearly, the aspect ratio has a significant effect on the temperature distributions. As shown in Figures 4g–4i, the aspect ratio in the third dimension also affects the temperature solution significantly at all of the three times. This indicates that heat conduction in 2-D/3-D rectangular blocks cannot be approximated using that in 1-D slabs.

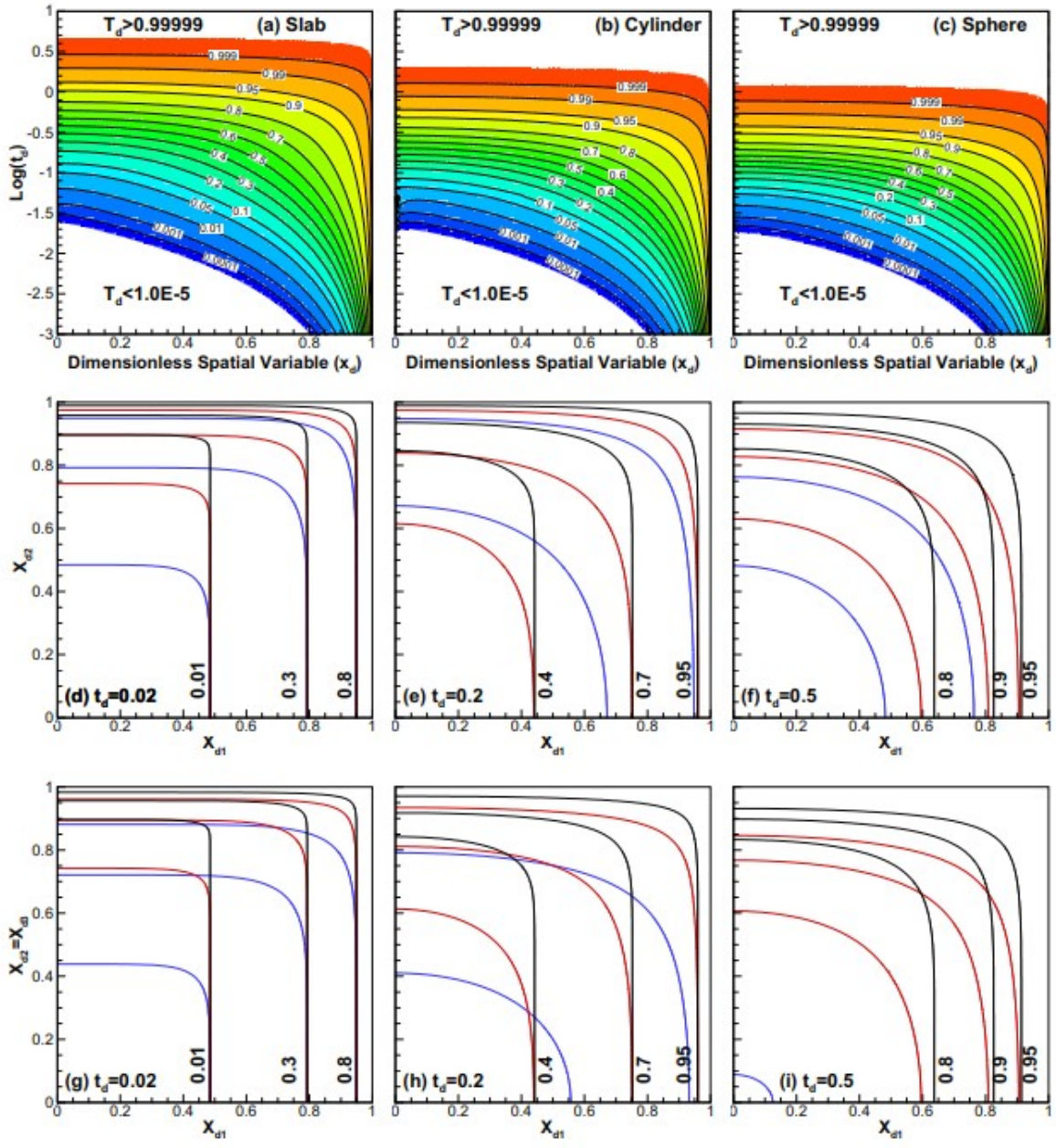

Figure 4

(a)–(c) Contour of dimensionless temperature (T_d) over the domain ($x_d, \log t_d$) for isotropic blocks (slab, cylinder, and sphere), (d)–(f) T_d contour over 2-D rectangles (x_{d1}, x_{d2}) at $t_d = 0.02,\ 0.2,\ 0.5$, and (g)–(i) T_d contour over 3-D rectangular parallelepipeds (x_{d1}, x_{d2}) with $x_{d3} = x_{d2}$ at $t_d = 0.02,\ 0.2,\ 0.5$. Note that the contour lines and their labels for the three rectangles with $R_{l2} =$ 1.0 (in blue lines), 0.5 (in red), and 0.2 (in black) and the three parallelepipeds with $(R_{l2}, R_{l3}) =$ (1.0, 1.0) (in blue), (0.5, 0.2) (in red), and (0.2, 0.1) (in black).

The temperature solution in 1-D slabs, 2-D rectangles, and 3-D rectangular parallelepipeds can be easily calculated using equation (8a–c) with high computational efficiency and accuracy. These solutions can support the refinement of numerical schemes (e.g., dual-porosity and multiple

interacting continuum [MINC] models), without the need of high-resolution numerical modeling (Cai et al., 2015; Lim & Aziz, 1995; Pruess & Narasimhan, 1985; Rubin, 2010).

4.2 Heat Flux Solutions

The flux equations in equation (11) and equation (13) with (16) or (17) are used for numerical evaluation of dimensionless cumulative flux for 1-D slab-like and 2-D/3-D rectangular blocks with the same aspect ratios used for the temperature solutions. The flux equations in equations (12) and 19 with $N=1$ are used to calculate the dimensionless transient flux for the same blocks, along with equations (12a) and (10a, 10b) for the exponential-series solution alone with $N=10,000$. All produce the same calculated transient flux over $t_d=$ [10^{-6}, 10]. Figure 5a shows the calculated dimensionless cumulative flux for all of these blocks, showing that the aspect ratios have significant effects on the calculated flux. Figures 5b and 5c show the dimensionless transient flux that varies over six orders of magnitude in the dimensionless time range [10^{-6}, 2]. Figure 5d shows that the maximum approximation error for a high-dimensional matrix block using a lower-dimensional one is less than 1.0% when the extradimension has an aspect ratio less than 0.01. For the aspect ratio of 0.1, the maximum approximation error can be as high as 10.0%. The maximum approximation error is calculated for the time domain [10^{-6}, 10]. Indeed, this relative error can be easily estimated using the flux equations directly. Practically, for an aspect ratio of 0.01, the corresponding dimension can be neglected for heat flux calculations.

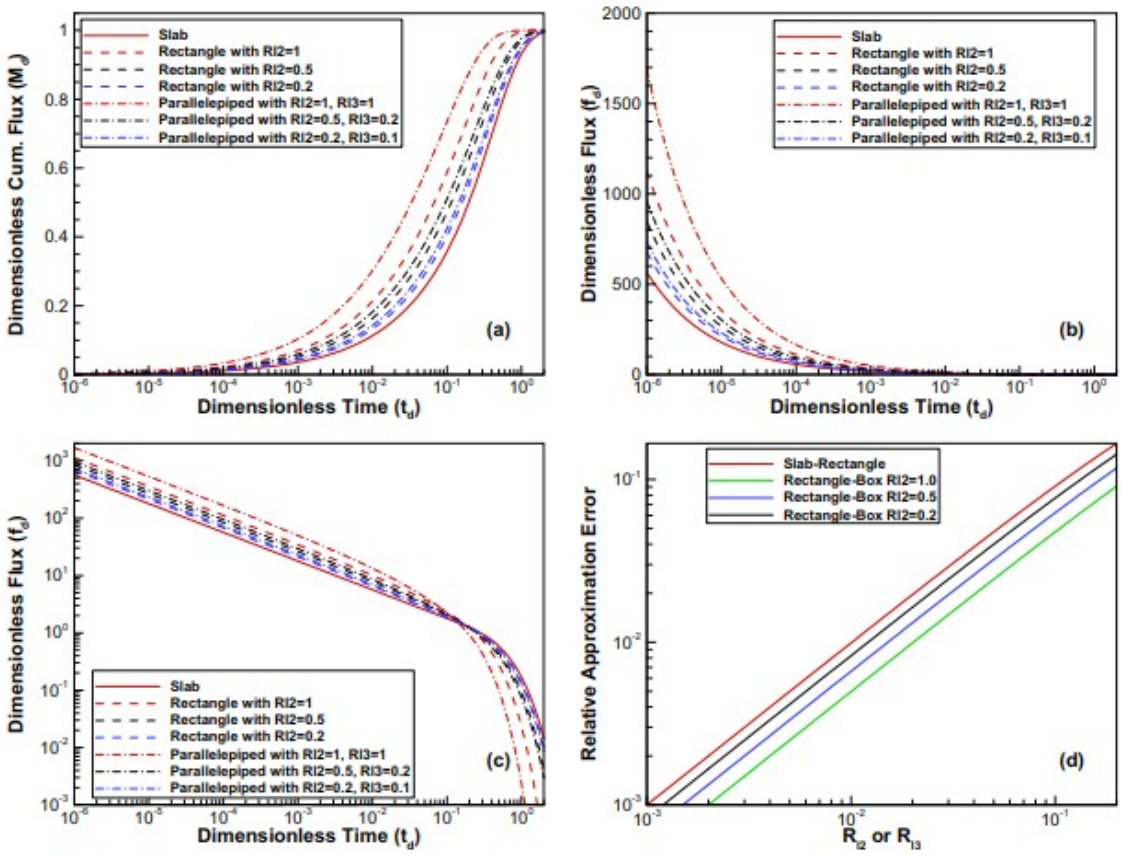

Figure 5

(a) Dimensionless cumulative flux (M_d), and (b) and (c) dimensionless transient flux (f_d) calculated using the combined solutions with time partitioning for 1-D slab-like and 2-D/3-D rectangular blocks with different aspect ratios, and (d) relative approximation error in M_d for a rectangle with small R_{I2} using a slab solution and for rectangular parallelepipeds with different R_{I2} and a small R_{I3} using rectangle solutions. Note that Figure 5b is in the log-linear scale and Figure 5c is in the log-log scale.

4.3 The Process of Equilibration

In this application, we are interested in the process of equilibration between an inner matrix block (immobile zone) and its surrounding high-permeability channel (mobile zone or fracture) whose outer boundary is impervious to hydraulic, thermal, and solute diffusion. The volumes of the immobile and mobile zones are denoted by V_m and V_f, respectively, and their volume ratio by $V_r=V_f/V_m$. For simplification, it is assumed that both the mobile and immobile zones have the same properties (e.g., porosity, grain density, and specific heat) with the same diffusivity and the former is well-mixed. For the thermal equilibrium between the mobile and immobile zones, a unit temperature change is introduced initially to the mobile zone, while the immobile zone is of initial temperature of 0. The governing equation for the dimensionless mobile-zone temperature (T_{df}) can be written

$$V_r \frac{\partial T_{df}}{\partial t_d} + (1-V_r) \frac{\partial T_{dav}}{\partial t_d} = 0, \quad (21a)$$

where T_{dav} is the dimensionless average temperature of the immobile zone. The thermal equilibration leads to time-dependent mobile-zone temperature, T_{df}, whose equilibrium value is V_r. Time convolution is used to calculate the average immobile-zone temperature:

$$T_{dav}(t_d) = \int_0^{t_d} T_{df}(t_d - \tau) f_d(\tau) d\tau = \int_0^{t_d} \frac{\partial T_{df}(t_d - \tau)}{\partial t_d} M_d(\tau) d\tau. \quad (21b)$$

Note that M_d and f_d are the dimensionless cumulative and transient heat flux with fixed boundary temperature of unity that can be calculated directly using the flux equations in equation (11) or (13) and equation (12) or (19), respectively. Equation (21b) can also be written in the Laplace domain.

Figure 6 shows the time-dependent dimensionless temperature in the mobile and immobile zone with the volume ratio $V_r = 0.1$ used for the same seven blocks. Again, the dimensionality and aspect ratios have a significant effect on the dimensionless temperature in both zones.

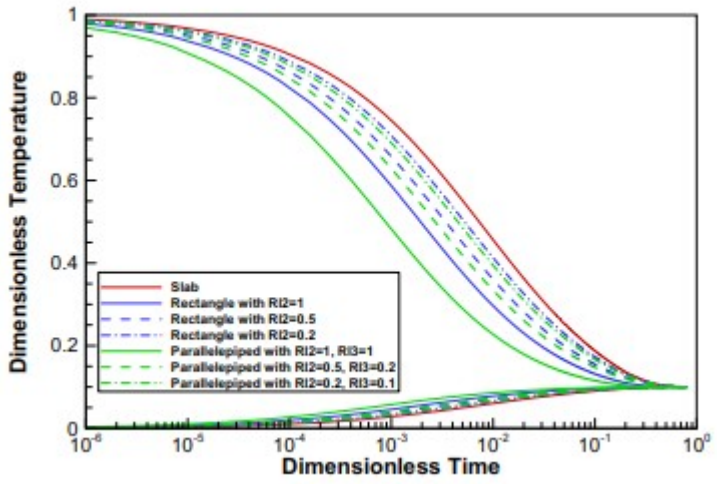

Figure 6

The process of thermal equilibration between the mobile (upper curves) and immobile zones (lower curves) with their dimensionless temperatures calculated using a volume ratio of 0.1 for the same seven matrix blocks of different dimensions and aspect ratios.

5 Conclusions

Following the complementary convergence properties of two types of infinite-series exact solutions of temperature/concentration in and heat/mass flux through the boundary of blocks of various shapes (sphere, cylinder, slab, square, cube, rectangle, and rectangular parallelepiped), we developed unified-form approximate solutions that contain the early-time and late-time solutions whose applicability is defined by a switchover dimensionless time. For the temperature/concentration solutions, the time partitioning of the early-time error-function-series solutions and the late-time exponential-series solutions produces rapid and uniform convergence of the combined solutions using the same number of terms, with the leading term for normal-

accuracy approximation (less than 0.3% relative error) and the first two terms of each series for high-accuracy approximation (less than 10^{-7} relative error). For 2-D/3-D rectangular blocks, rapid and uniform convergence of the approximate solutions is achieved using the same time partitioning based on the individual dimensionless time (t_{di}, t_{d0}^{T}) for different spatial directions and the product of their combined 1-D slab solutions.

We also achieved rapid and uniform convergence of the combined heat/mass flux equations with the early and late-time solutions for 1-D slab-like and 2-D/3-D rectangular blocks. In these flux equations, the product of the combined 1-D slab solution for each direction using the same (t_{di}, t_{d0}) time partitioning is used to guarantee rapid and uniform convergence for normal and high-accuracy approximations. This product form of flux equations is fast and very efficient for numerical evaluations. For the second form, we derived the early-time flux equations for 2-D/3-D rectangular blocks that are presented in terms of the three-term polynomials for normal-accuracy approximation; the three coefficients of the polynomials depend only on the dimensionless area-to-volume ratio and aspect ratios. To honor accepted physical insights into heat flux, we employ the time-partitioning of the early and the late-time solutions based on (t_d, t_{d0}) and a nonuniform convergence is achieved as additional exponential terms for the late-time solutions are needed for highly anisotropic blocks. For squares and cubes, the two forms of flux equations have the same convergence properties as for 1-D slabs. The second, nonproduct form of the flux equations with normal-accuracy approximation can be directly used to couple local conduction/diffusion with modeling large-scale heat/mass transfer in fractured or heterogeneous porous media.

Acknowledgments

This work was supported by the Assistant Secretary for Fossil Energy, Office of Sequestration, Hydrogen, and Clean Coal Fuels, of the U.S. Department of Energy under contract DE-AC02-05CH11231 to Lawrence Berkeley National Laboratory (LBNL) through grant FE0023323 to Princeton University and through the Regional Carbon Sequestration Partnership Program Award DE-FC26-05NT42587 to the Big Sky Carbon Sequestration Partnership (BSCSP). This work was also partially supported by the California Energy Commission (CEC) through an Electric Program Investment Charge (EPIC) funding award on geothermal energy to LBNL under agreement EPC-16-022. We note that there are no data sharing issues because all of the numerical data shown in the figures are in fact produced by the developed approximate analytical solutions in the paper. The computer codes used to calculate these solutions are available from the authors upon request.

Appendix A: Derivation of the Flux Equation for Rectangles and Rectangular Parallelepipeds

In the following derivation of the flux equations for 2-D (or 3-D) rectangular blocks, we take advantage of the product of 1-D (complementary)

temperature solutions T' for slabs with $x_1 \in [0, 2l_1]$, $x_2 \in [0, 2l_2]$ (and $x_3 \in [0, 2l_3]$), with a unit initial temperature and zero temperature fixed at all block boundary surfaces (Crank, 1975, p. 25). For the heat conduction with a unit boundary temperature and zero initial temperature (Carslaw & Jaeger, 1959, p. 171), we have $T'=1-T$ and $q'=-q$, where q' and q are the heat flux for T' and T, respectively. The shift of the coordinates from section 2 is used to facilitate the integration of heat flux over the boundary surfaces.

For a 2-D rectangular block, following Carslaw and Jaeger (1959, p. 171), we have the error-function-based temperature solutions for the early-time flux calculations considering only one quarter of the rectangle:

$$T'=\operatorname{erf}\frac{x_1}{2\sqrt{Dt}}\operatorname{erf}\frac{x_2}{2\sqrt{Dt}},\ x_1 \in [0, l_1] \text{ and } x_2 \in [0, l_2]. \quad \text{(A1)}$$

The flux of heat at the point (0, x_2) of the rectangle edge is

$$q'_1=-K\left.\frac{\partial T'}{\partial x_1}\right|_{x_1=0}=\frac{-K}{\sqrt{\pi Dt}}\operatorname{erf}\frac{x_2}{2\sqrt{Dt}}. \quad \text{(A2)}$$

The difference between equation A2 and the heat flux for a semi-infinite block with boundary at $x_1=0$ is

$$\Delta q'_1=\frac{K}{\sqrt{\pi Dt}}\operatorname{erfc}\frac{x_2}{2\sqrt{Dt}}. \quad \text{(A3)}$$

Thus, the total differential heat flux for the entire edge ($x_1=0$) of the rectangle quarter is

$$\Delta Q'_1=\int_0^{l_2}\frac{K}{\sqrt{\pi Dt}}\operatorname{erfc}\frac{x_2}{2\sqrt{Dt}}dx_2=\frac{2K}{\pi}. \quad \text{(A4)}$$

Note that equation A4 is valid only for all times before the arrival of the temperature front at $2l_1$. By summing the semi-infinite flux and the differential flux along the two rectangular edges $x_1=0$, and $x_2=0$, we obtain the total boundary flux, Q':

$$Q'=\left(Q'_1+Q'_2\right)+\left(\Delta Q'_1+\Delta Q'_2\right)=-\frac{K}{\sqrt{\pi Dt}}(l_1+l_2)+\frac{4K}{\pi}. \quad \text{(A5)}$$

The first term in equation A5 is for the rectangle edges that act like a semi-infinite block with a length of l_1+l_2, without interference at the rectangle corner. The second term is for the total differential flux that is equal for each edge of the rectangle quarter.

The heat flux per unit area, defined by the ratio of the total boundary flux to the thermal energy stored in the rectangle quarter, for the heat-conduction problem in sections 2 and 3 can be written

$$f_d=\frac{-Q'}{\rho c l_1 l_2}=\frac{D}{l_1^2}\left(\frac{1+R_{l2}}{\sqrt{\pi t_d}}-\frac{4}{\pi}R_{l2}\right), \quad \text{(A6)}$$

where ρ is the solid density and c is the specific heat of the solid. Following the definition of the dimensionless cumulative flux, we have

$$M_d = \int_0^t f_d dt = \frac{-\int_0^t Q' dt}{\rho c l_1 l_2} = \frac{2(1+R_{l2})}{\sqrt{\pi}}\sqrt{t_d} - \frac{4}{\pi}R_{l2}t_d. \quad \text{(A7)}$$

For a rectangular parallelepiped, the error-function-based temperature solution for the early-time flux calculations is

$$T' = \operatorname{erf}\frac{x_1}{2\sqrt{Dt}}\operatorname{erf}\frac{x_2}{2\sqrt{Dt}}\operatorname{erf}\frac{x_3}{2\sqrt{Dt}},\ x_1 \in [0, l_1], x_2 \in [0, l_2] \text{ and } x_3 \in [0, l_3]. \quad \text{(A8)}$$

The flux of heat at the point (0, x_2, x_3) of the parallelepiped surface is

$$q_1' = -K\left.\frac{\partial T'}{\partial x_1}\right|_{x_1=0} = \frac{-K}{\sqrt{\pi Dt}}\operatorname{erf}\frac{x_2}{2\sqrt{Dt}}\operatorname{erf}\frac{x_3}{2\sqrt{Dt}}. \quad \text{(A9)}$$

The difference between equation A9 and the heat flux for a semi-infinite block is

$$\Delta q_1' = \frac{K}{\sqrt{\pi Dt}}\left(1 - \operatorname{erf}\frac{x_2}{2\sqrt{Dt}}\operatorname{erf}\frac{x_3}{2\sqrt{Dt}}\right). \quad \text{(A10)}$$

Thus, the total differential heat flux for the entire plane ($x_1 = 0$) of the 1/8 parallelepiped is

$$\Delta Q_1' = \frac{K}{\sqrt{\pi Dt}}\int_0^{l_3}\int_0^{l_2}\left(\operatorname{erfc}\frac{x_2}{2\sqrt{Dt}} + \operatorname{erfc}\frac{x_3}{2\sqrt{Dt}} - \operatorname{erfc}\frac{x_2}{2\sqrt{Dt}}\operatorname{erfc}\frac{x_3}{2\sqrt{Dt}}\right)dx_2 dx_3$$
$$= \frac{2K}{\pi}(l_2 + l_3) - \frac{4K}{(\sqrt{\pi})^3}\sqrt{Dt}. \quad \text{(A11)}$$

Note that equation A11 is valid only for all times before the arrival of the temperature front at $2l_1$. By summing the semi-infinite flux and differential flux over the three block planes at $x_1 = 0$, $x_2 = 0$, and $x_3 = 0$, we obtain the total boundary flux, Q':

$$Q' = \left(Q_1' + Q_2' + Q_3'\right) + \left(\Delta Q_1' + \Delta Q_2' + \Delta Q_3'\right)$$
$$= -\frac{K}{\sqrt{\pi Dt}}(l_2 l_3 + l_1 l_3 + l_1 l_2) + \frac{4K}{\pi}(l_1 + l_2 + l_3) - \frac{12K}{(\sqrt{\pi})^3}\sqrt{Dt}. \quad \text{(A12)}$$

Again, the first term on the right-hand side of equation A12 is for the rectangular planes that act like a semi-infinite block with a total surface area, without interference at the parallelepiped corner, while the last two terms are for the differential flux for the entire 1/8 parallelepiped.

The heat flux per unit volume, defined by the ratio of the total boundary flux to the thermal energy stored in the 1/8 rectangular parallelepiped, for the heat-conduction problems in sections 2 and 3 can be written

$$f_d = \frac{-Q'}{\rho c l_1 l_2 l_3} = \frac{D}{l_1^2}\left\{\frac{1 + R_{l2} + R_{l3}}{\sqrt{\pi t_d}} - \frac{4}{\pi}(R_{l2} + R_{l3} + R_{l2}R_{l3}) + \frac{12}{\pi^{2/3}}R_{l2}R_{l3}\sqrt{t_d}\right\}. \quad \text{(A13)}$$

Again, following the definition of M_d, we have

$$M_d = \int_0^t f_d dt = \frac{-\int_0^t Q' dt}{\rho c l_1 l_2 l_3} = \frac{2(1+R_{l2}+R_{l3})}{\sqrt{\pi}}\sqrt{t_d} - \frac{4}{\pi}(R_{l2} + R_{l3} + R_{l2}R_{l3})t_d + \frac{8}{\pi^{\frac{3}{2}}}R_{l2}R_{l3}t_d^{\frac{3}{2}}. \quad \text{(A14)}$$

References

Barenblatt, G. E., Zheltov, I. P., & Kochina, I. N. (1960). Basic concepts in the theory of homogeneous liquids in fissured rocks. *Journal of Applied Mathematics and Mechanics*, 24(5), 1286– 1303. https://doi.org/10.1016/0021-8928(60)90107-6

Beck, J. V., & Cole, K. D. (2007). Improving convergence of summations in heat conduction. *International Journal of Heat and Mass Transfer*, 50, 257–268. https://doi.org/10.1016/j.ijheatmasstransfer.2006.06.032

Beck, J. V., Cole, K. D., Haji-Sheikh, A., & Litkouhi, B. (1992). *Heat conduction using Green's functions*. New York, NY: Hemisphere Publishing Corporation.

Beck, J. V., Haji-Sheikh, A., Amos, D. E., & Yen, D. H. Y. (2004). Verification solution for partial heating of rectangular solids. *International Journal of Heat and Mass Transfer*, 47, 4243– 4255. https://doi.org/10.1016/j.ijheatmasstransfer.2004.04.021

Beck, J. V., McMasters, R., Dowding, K. J., & Amos, D. E. (2006). Intrinsic verification methods in linear heat conduction. *International Journal of Heat and Mass Transfer*, 49, 2984– 2994. https://doi.org/10.1016/j.ijheatmasstransfer.2006.01.045

Beck, J. V., Wright, N. T., Haji-Sheikh, A., Cole, K. D., & Amos, D. E. (2008). Conduction in rectangular plates with boundary temperatures specified. *International Journal of Heat and Mass Transfer*, 51, 4676– 4690. https://doi.org/10.1016/j.ijheatmasstransfer.2008.02.020

Becker, M. W., & Charbeneau, R. J. (2000). First-passage-time transfer functions for groundwater tracer tests conducted in radially convergent flow. *Journal of Contaminant Hydrology*, 40, 299– 310. https://doi.org/10.1016/S0169-7722(99)00061-3

Brusseau, M. L., Jessup, R. E., & Rao, P. S. C. (1989). Modeling the transport of solutes influenced by multiprocess nonequilibrium. *Water Resources Research*, 25(9), 1971– 1988. https://doi.org/10.1029/WR025i009p01971

Cai, L., Ding, D.-Y., Wang, C., & Wu, Y.-S. (2015). Accurate and efficient simulation of fracture-matrix interaction in shale gas reservoirs. *Transport in Porous Media*, 107, 305– 320. https://doi.org/10.1007/s11242-014-0437-x

Carrera, J., Sanchez-Vila, X., Benet, I., Medina, A., Galarza, G., & Guimera, J. (1998). On matrix diffusion: Formulations, solution methods and qualitative effects. *Hydrogeology Journal*, 6(1), 178– 190. https://doi.org/10.1007/s100400050143

Carslaw, H. S., & Jaeger, J. C. (1959). *Conduction of heat in solids* (2nd ed.). Oxford, UK: Clarendon.

Cihan, A., Zhou, Q., & Birkholzer, J. T. (2011). Analytical solutions for pressure perturbation and fluid leakage through aquitards and wells in a

multilayered system. *Water Resources Research*, 47, W10504. https://doi.org/10.1029/2011WR010721

Coats, K. H., & Smith, B. D. (1964). Dead-end pore volume and dispersion in porous media. *Society of Petroleum Engineers Journal*, 4(1), 73– 84. https://doi.org/10.2118/647-PA

Cole, K. D., & Yen, D. H. Y. (2001). Green's functions, temperature, and heat flux in the rectangle. *International Journal of Heat and Mass Transfer*, 44(20), 3883– 3894. https://doi.org/10.1016/S0017-9310(01)00040-0

Crank, J. (1975). *The mathematics of diffusion* (2nd ed.). New York, NY: Oxford University Press.

Crittenden, P. E., & Cole, K. D. (2002). Fast-converging steady-state heat conduction in the rectangular parallelepiped. *International Journal of Heat and Mass Transfer*, 45, 3585– 3596. https://doi.org/10.1016/S0017-9310(02)00066-2

Dykhuizen, R. C. (1990). A new coupling term for dual-porosity models. *Water Resources Research*, 26(2), 351– 356. https://doi.org/10.1029/WR026i002p00351

Guan, J., Molz, F. J., Zhou, Q., Liu, H.-H., & Zheng, C. (2008). Behavior of the mass transfer coefficient during the MADE-2 experiment: New insights. *Water Resources Research*, 44, W02423. https://doi.org/10.1029/2007WR006120

Haggerty, R., Fleming, S. W., Meigs, L. C., & McKenna, S. A. (2001). Tracer tests in a fractured dolomite: 2. Analysis of mass transfer in single well injection-withdrawal tests. *Water Resources Research*, 37(5), 1113– 1128. https://doi.org/10.1029/2000WR900334

Haggerty, R., & Gorelick, S. M. (1995). Multiple-rate mass transfer for modeling diffusion and surface reactions in media with pore-scale heterogeneity. *Water Resources Research*, 31(10), 2383– 2400. https://doi.org/10.1029/95WR10583

Haggerty, R., Harvey, C. F., von Schwerin, C. F., & Meigs, L. (2004). What controls the apparent timescale of solute mass transfer in aquifers and soils? A comparison of experimental results. *Water Resources Research*, 40, W01510. https://doi.org/10.1029/2002WR001716

Haggerty, R., McKenna, S. A., & Meigs, L. C. (2000). On the late-time behavior of tracer test breakthrough curves. *Water Resources Research*, 36(12), 3467– 3479. https://doi.org/10.1029/2000WR900214

Hahn, D. W., & Ozisik, M. N. (2012). *Heat conduction* (3rd ed.). Hoboken, NJ: John Wiley.

Heisler, M. P. (1947). Temperature charts for induction and constant-temperature heating. *ASME Transactions*, 69, 227– 236.

Holman, J. P. (1990). *Heat transfer* (7th ed.). New York, NY: McGraw-Hill.

Jung, Y., & Pruess, K. (2012). A closed-form analytical solution for thermal single-well injection-withdrawal tests. *Water Resources Research*, 48, W03504. https://doi.org/10.1029/2011WR010979

Lauwerier, H. A. (1955). The transport of heat in an oil layer caused by the injection of hot fluid. *Applied Scientific Research, Section A*, 5(2–3), 145–150. https://doi.org/10.1007/BF03184614

Lim, K. T., & Aziz, K. (1995). Matrix-fracture transfer shape factors for dual-porosity simulators. *Journal of Petroleum Science and Engineering*, 13, 169–178. https://doi.org/10.1016/0920-4105(95)00010-F

Maloszewski, P., & Zuber, A. (1985). On the theory of tracer experiments in fissured rocks with a porous matrix. *Journal of Hydrology*, 79, 333– 358. https://doi.org/10.1016/0022-1694(85)90064-2

Maloszewski, P., & Zuber, A. (1990). Mathematical modeling of tracer behavior in short-term experiments in fissured rocks. *Water Resources Research*, 26(7), 1517– 1528. https://doi.org/10.1029/WR026i007p01517

Maloszewski, P., & Zuber, A. (1993). Tracer experiments in fractured rocks: Matrix diffusion and the validity of models. *Water Resources Research*, 29(8), 2723– 2735. https://doi.org/10.1029/93WR00608

March, R., Doster, F., & Geiger, S. (2016). Accurate early-time and late-time modeling of countercurrent spontaneous imbibition. *Water Resources Research*, 52, 6263– 6276. https://doi.org/10.1002/2015WR018456

McMasters, R. L., Dowding, K., Beck, J. V., & Yen, D. (2002). Methodology to generate accurate solutions for verification in transient three-dimensional heat conduction. *Journal of Numerical Heat Transfer, Part B*, 41(6), 521– 541. https://doi.org/10.1080/10407790190053761

Moench, A. F. (1984). Double-porosity models for a fissured groundwater reservoir with fracture skin. *Water Resources Research*, 20(7), 831– 846. https://doi.org/10.1029/WR020i007p00831

Moench, A. F. (1989). Convergent radial dispersion: A Laplace transform solution for aquifer tracer testing. *Water Resources Research*, 25(3), 439–447. https://doi.org/10.1029/WR025i003p00439

Moench, A. F. (1991). Convergent radial dispersion: A note on evaluation of the Laplace transform solution. *Water Resources Research*, 27(12), 3261–3264. https://doi.org/10.1029/91WR02301

Moench, A. F. (1995). Convergent radial dispersion in a double-porosity aquifer with fracture skin: analytical solution and application to a field experiment in fractured chalk. *Water Resources Research*, 31(8), 1823–1835. https://doi.org/10.1029/95WR01275

Newman, A. B. (1936). Heating and cooling rectangular and cylindrical solids. *Industrial & Engineering Chemistry*, 28(5), 545– 548. https://doi.org/10.1021/ie50317a010

Pruess, K., & Narasimhan, T. N. (1985). A practical method for modeling fluid and heat flow in fractured porous media. *Society of Petroleum Engineers Journal*, 25(1), 14– 26. https://doi.org/10.2118/10509-PA

Reimus, P., Pohll, G., Mihevc, T., Chapman, J., Haga, M., Lyles, B., … Sanders, P. (2003). Testing and parameterizing a conceptual model for solute transport in a fractured granite using multiple tracers in a forced-gradient test. *Water Resources Research*, 39(12), 1356. https://doi.org/10.1029/2002WR001597

Rubin, B. (2010). *Accurate simulation of non-Darcy flow in stimulated fractured shale reservoirs*. Paper presented at the SPE Western Regional Meeting (SPE 132093), Anaheim, CA.

Silva, O., Carrera, J., Dentz, M., Kumar, S., Alcolea, A., & Willmann, M. (2009). A general real-time formulation for multi-rate mass transfer problems. *Hydrology and Earth System Sciences*, 13, 1399– 1411. https://doi.org/10.5194/hess-13-1399-2009

Sudicky, E. A., & Frind, E. O. (1982). Contaminant transport in fractured porous media: analytical solutions for a system of parallel fractures. *Water Resources Research*, 18(7), 1634– 1642. https://doi.org/10.1029/WR018i006p01634

Tang, D. H., Frind, E. O., & Sudicky, E. A. (1981). Contaminant transport in fractured porous media: analytical solution for a single fracture. *Water Resources Research*, 17(3), 555– 564. https://doi.org/10.1029/WR017i003p00555

van Genuchten, M. T., & Dalton, F. N. (1986). Models for simulating salt movement in aggregated field soils. *Geoderma*, 38, 165– 183. https://doi.org/10.1016/0016-7061(86)90013-3

van Genuchten, M. T., & Wierenga, P. J. (1976). Mass transfer studies in sorbing porous media: 1. Analytical solutions. *Soil Science Society of America Journal*, 40(4), 473– 480. https://doi.org/10.2136/sssaj1976.03615995004000040011x

Warren, J. P., & Root, P. J. (1963). The behavior of naturally fractured reservoirs. *Society of Petroleum Engineers Journal*, 3(3), 244– 255. https://doi.org/10.2118/426-PA

Willmann, M., Carrera, J., & Sánchez-Vila, X. (2008). Transport upscaling in heterogeneous aquifers: what physical parameters control memory functions? *Water Resources Research*, 44, W12437. https://doi.org/10.1029/2007WR006531

Yen, D. H. Y., Beck, J. V., McMasters, R. L., & Amos, D. E. (2002). Solution of an initial-boundary value problem for heat conduction in a parallelepiped by time partitioning. *International Journal of Heat and Mass Transfer*, 45, 4267–4279. https://doi.org/10.1016/S0017–9310(02)00145-X

Zhang, Y., Pan, L., Pruess, K., & Finsterle, S. (2011). A time-convolution approach for modeling heat exchange between a wellbore and surrounding formation. *Geothermics*, 40, 261– 266. https://doi.org/10.1016/j.geothermics.2011.08.003

Zhou, Q., Birkholzer, J. T., & Tsang, C.-F. (2009). A semi-analytical solution for large-scale injection-induced pressure perturbation and leakage in a laterally bounded aquifer-aquitard system. *Transport in Porous Media*, 78(1), 127–148. https://doi.org/10.1007/s11242-008-9290-0

Zhou, Q., Liu, H.-H., Bodvarsson, G. S., & Molz, F. J. (2006). Evidence of multi-process matrix diffusion in a single fracture from a field tracer test. *Transport in Porous Media*, 63(3), 473– 487. https://doi.org/10.1007/s11242-005-1123-9

Zhou, Q., Liu, H.-H., Molz, F. J., Zhang, Y., & Bodvarsson, G. S. (2007). Field-scale effective matrix diffusion coefficient for fractured rock: Results from literature survey. *Journal of Contaminant Hydrology*, 93, 161– 187. https://doi.org/10.1016/j.jconhyd.2007.02.002

Zhou, Q., Oldenburg, C. M., Spangler, L. H., & Birkholzer, J. T. (2017). Approximate solutions for diffusive fracture-matrix transfer: Application to storage of dissolved CO_2 in fractured rocks. *Water Resources Research*, 53, 1746– 1762. https://doi.org/10.1002/2016WR019868